Hindawi
Advances in Meteorology
Volume 2019, Article ID 4631609, 15 pages
https://doi.org/10.1155/2019/4631609

Research Article

Seasonal and Regional Differences in Extreme Rainfall Events and Their Contribution to the World's Precipitation: GPM Observations

Shailendra Kumar, Yamina Silva, Aldo S. Moya-Álvarez, and Daniel Martínez-Castro

Instituto Geofisico del Peru, Calle Badajoz 169, Urb. Mayorazgo IV Etapa, Ate, Lima, Peru

Correspondence should be addressed to Shailendra Kumar; shailendrak89@gmail.com

Received 15 January 2019; Revised 19 March 2019; Accepted 2 May 2019; Published 30 May 2019

Guest Editor: Jongho Kim

In the present study, five-year of precipitation features (PFs) datasets, based on Global Precipitation Measurement (GPM), are used to investigate the global and regional characteristics of extreme rainfall events (EREs). The EREs are defined based on the PFs area, depth (maximum height of radar reflectivity), and the rain rate and called them largest, deepest, and intense EREs, respectively. The EREs are divided into top 10%, 1%, 0.1%, and 0.01% based on their frequency of occurrences. It is observed that occurrences of EREs belonging to less than top 0.01% EREs follow the tropical rainfall climatology over the tropics based on all the parameters. Subtropical oceanic areas consist of a higher frequency of largest EREs, whereas tropical land areas consist of the higher number of deepest EREs. The most intense EREs (top 0.01%) are uniformly distributed over tropical areas and subtropical oceans, and spatial distribution shows that a deepest ERE belongs to intense EREs in the tropical land areas. Large differences between the precipitation contribution from the largest and deepest EREs are seen; for example, the top 1% of largest EREs contribute to ~80.7% of Earth's precipitation, whereas the corresponding percentage for deepest EREs is only 53%. On the regional and seasonal scale, South Asia (SAsia) and South America (SA) nearly show common features, as oceanic and land areas consist of largest and deepest EREs, respectively, and contribute to higher precipitation. Subtropical latitudes over South America, including Sierra de Cordoba and La Plata basin, consist of deepest and intense EREs and match with those of the Indo-Gangetic plain over South Asia, which also shows the similar characteristics. EREs based on various parameters are strongly linked over SAsia compared to SA. For example, the largest top 10% EREs have a higher probability to be part of the top 10% deepest and intense EREs over SAsia. The seasonal and regional water budget reveals different characteristics, as in the southern hemisphere, the deeper EREs contribute to the higher fraction of rainfall, but over SAsia, the shallower EREs could also contribute to significant rainfall.

1. Introduction

Mesoscale convective systems (MCS) play a vital role in tropical large-scale circulation (e.g., [1, 2]) and Earth's water budget, as most of Earth's rainfall comes from them [3]. Therefore, it is very important to understand them globally, seasonally, and regionally. The extreme rainfall events (EREs) are related to atmospheric/weather conditions [4]. Some common EREs are associated with MCSs [5] and could produce a copious amount of rainfall over the tropical land and oceanic areas. Because of their large impact on the Earth's energy and water budget, the scientific community has studied their properties in many ways, including field campaigns (e.g., GATE, Monsoon Experiment (MONEX), TOGA COARE, DYNAMO, and COPE), satellite observations, and numerical modeling (e.g., [2, 6–9]). Passive microwave radiometers can detect the strength of ice scattering signals, whereas lightning data were used to identify the global distribution of storms [10–13]. The Tropical Rainfall Measuring Mission (TRMM) satellite was launched in 1997, consists of multiple sensors, and provides the three-dimensional structure of precipitation [14] from space.

The TRMM-based precipitation features (PFs) consist of valuable information of the precipitation, such as its depth, area, convective-stratiform fraction, rain rate (RR), and volumetric contribution to rainfall [15, 16]. Past studies detected the various properties of precipitation over the tropics and subtropics using the TRMM sensors [17–31], including their vertical characteristics, diurnal cycle, convective-stratiform separation, and other properties. Extreme and intense convection is defined using the radar reflectivity as a threshold in many studies over different tropical areas [24, 26, 27, 29, 30, 32]. For example, the maximum height of 40 dBZ is used as a convective proxy [23], and based on the criteria, it is observed that some of the most intense thunderstorms occur over the tropical land areas [33]. TRMM data are used to investigate the scale-based precipitation systems over the tropical globe [34], and the precipitation systems are classified into small ($<100\,km^2$) and large ($>10000\,km^2$) ones. The observations revealed that small precipitation systems do not show much diurnal variation, whereas large precipitation systems mostly occur in the afternoon. The geographical locations of 1000 extreme precipitation events with the highest volumetric rainfall amount showed that these events are unevenly distributed and mostly occur near South America and associated with the tropical cyclone [35]. Hamada et al. [35] defined the intense rainfall events using RR ($mm\,h^{-1}$). They considered the RR greater than 99.99 percentile in each $2.5^\circ \times 2.5^\circ$ grid box over the tropical areas [35] and showed that most of the volumetric higher rainfall events are associated with cyclones. A weak linkage is observed between the largest precipitating systems and their corresponding top height [4]. Table 1 lists the past studies where intense and extreme rainfall events are studied using the TRMM data.

Monsoon domains are defined based on the annual and seasonal rainfall criteria [37]. Monsoon domains consist of more than 70% of the total annual rainfall during local summer seasons. Based on the mentioned criteria, monsoon domains are defined over South East South Asia, Indonesia-Australia, Northern and Southern Africa, and North and South America. In the past, various studies were carried out to investigate the rainfall characteristics, such as monsoon circulation pattern, intraseasonal variation, and mesoscale convection (e.g., [37–41]). However, there are very few studies that have been carried out to understand the distribution and characteristics of EREs globally, regionally, and seasonally. The multiscale climatology of large, deep, and intense rain events will improve the estimation of rainfall by using microwave radiometers [42, 43]. The main objectives of the present study are to investigate the global view of the spatial distribution of EREs and their role/contribution to global precipitation. We also selected two monsoon seasons, namely, Indian summer monsoon (June to September, JJAS) and Austral summer monsoon (December to March, DJFM) over South Asia (SAsia, 55°E–110°E, 0–35°N) and South America (SA, 80°W–35°W, 10°N–55°S) to investigate the regional and seasonal distribution of EREs and their contribution in regional precipitation during two monsoon seasons. For this, we used the PFs from the Global Precipitation Measurement (GPM) observations. The core satellite of the GPM was launched in February 2014 and consists of a dual-polarized radar (DPR) and a microwave imager (GMI). In summary, the main objectives of the present study are to answer the following questions:

(a) What is the spatial distribution of the largest, deepest, and intense EREs on the Earth using 4-year GPM data (April 2014–December 2017) and their importance in world precipitation?

(b) What are the regional differences of occurrence of these EREs during two monsoon seasons over SAsia and SA, and how important is the contribution of these EREs relative to the seasonal and regional precipitation?

(c) How are these EREs interlinked based on their size, depth, and rainfall intensity during Indian and Austral summer monsoon seasons over SAsia and SA, respectively?

The paper is organized as follows. Section 2 provides a summary of the data used in the present study and introduces the method for defining EREs. Section 3 describes the global distribution of EREs and their characteristics on a global, regional, and seasonal scale. Summary and concluding remarks are given in section 4.

2. Global Precipitation Measurement (GPM), Precipitation Features (PFs), and Extreme Rainfall Events (EREs)

GPM, a successor of TRMM, is a joint multisatellite mission by NASA and the Japanese Space Agency, which provides the global information of precipitation [44]. The core observatory of GPM has a DPR and an advanced passive microwave radiometer, which measures the three-dimensional characteristics of precipitation. GPM covers the area between 65°S and 65°N compared to the TRMM, whose span was only 36°S–36°N. In the present study, we used the PFs based on GPM DPR and passive microwave radiometers sensors (http://atmos.tamucc.edu/trmm/data.html#datadownload) [33]. The PFs are defined as the connected pixels of PR beams with near-surface rain rate $>0.1\,mm\,h^{-1}$ [33]. These PFs are further used to extract the characteristics of EREs on a global, regional, and seasonal scale. Here, the extremely large, deep, and intense EREs are identified and their properties such as echo top height, area, and RR are explored. Last, the fractions of precipitation contributed by these EREs are estimated for comparing the global and regional precipitation budgets.

Basically, GPM based PFs are used to characterize the EREs based on various parameters [33]. Liu and Zipser [33] classified the EREs into the top 10%, 1%, 0.1%, and 0.01% based on their area and top height using one year of GPM data. We followed the methodology used in [33] and defined three types of EREs, namely, the largest, deepest and intense EREs based on the area, top height, and RR of PFs, respectively (Table 2). Basically, we plotted the cumulative frequency distribution (CDF) of all the parameters and then

Table 1: Past studies considered to investigate the extreme rainfall events using the TRMM satellite.

Reference	Definition of extreme events
Zipser et al. [23]	Maximum height of 40 dBZ; minimum brightness temperature at 37 and 85 GHz; higher lightning flash rate
Houze et al. [24]	
Romatschke and Houze [32]	Deep intense convective echoes (40 dBZ echo reaching heights>10 km)
Romatschke et al. [32]	Wide intense convective echoes (40 dBZ echo > 1000 km^2 in horizontal dimension)
Rasmussen and Houze [36]	
Hirose et al. [34]	Small (<100 km^2) and large (>10000 km^2) precipitation systems
Hamada et al. [35]	Rain rate (mm h^{-1}) higher than the 99.99 percentile in each 2.5° × 2.5° grid box over the tropical areas
Bhat and Kumar [26]	Radar reflectivity > 20 dBZ at 12 km and top 5% radar reflectivity at 3 and 8 km
Kumar and Bhat [27]	
Kumar [28, 29]	Radar reflectivity > 40 dBZ at 3 km
Hamada et al. [4]	Rain rate (mm h^{-1}) higher than the 99.99 percentile in each 2.5° × 2.5° grid box over the tropical areas
Liu and Zipser [34]	Divided the PFs into top 10%, 1%, 0.1%, and 0.01% group based on the area and maximum height of PFs

Table 2: Definition of extreme rainfall events.

Types	Parameters
(1) Largest EREs	PFs area and volumetric area
(2) Deepest EREs	Maximum height of 20 and 40 dBZ (MH20 and MH40)
(3) Intense EREs	Rain rate (RR)

divided them into the top 10%, 1%, 0.1%, and 0.01% based on their number of occurrences (Supplementary Figure 1). The largest EREs are defined based on the area of PFs (km^2) and area of volumetric rainfall contribution (km^2 mm h^{-1}), whereas the deepest EREs are defined based on the maximum height of 20 dBZ (MH20, in km) and the maximum height of 40 dBZ (MH40, in km). The intense EREs are defined based on the RR (in mm h^{-1}), and the parameters are mentioned in Table 2, which shows the definition of various kinds of EREs used in the present study.

3. Results and Discussions

3.1. Global Distribution of Extreme Rainfall Events. Figure 1 shows the spatial distribution of the largest EREs based on the area of PFs (top 10%, top 1%, top 0.1%, and top 0.01%). The first three panels (Figures 1(a)–1(c)) show the distribution of the largest EREs in each 1° × 1° box, whereas Figure 1(d) shows the actual geographical locations of the top 0.1% (green color) and the top 0.01% largest EREs (magenta color). The spatial distribution of less than 99.99% largest EREs follows the total rainfall climatology (Figures 1(a)–1(c)), and the higher number of EREs are observed over the tropical belt and at high latitudes over oceanic areas [45–47]. The largest EREs (top 0.01%) occur over the oceanic areas beyond the tropics. The most valuable benefit from GPM observations are apparent; because of their scanning at higher latitudes, it is clearly observed that mid latitude and high latitude over oceans (beyond 35°S and 35°N) consist of the largest EREs. Figures 2(a)–2(c) and 3(a)–3(c) show the spatial distribution of the deepest EREs in a 1° × 1° box based on MH20 and MH40, respectively, and they also follow the long-term rainfall climatology. Tropical oceanic areas and high latitudes (beyond 38°) consist of shallow EREs (up to 5 km, Figure 2(a)) and are consistent with the TRMM observation [31]. Tropical land-dominated areas such as the Indo-Gangetic plain (IGP), central India, Maritime Continent (MC), north Australia (NAUS), and central South America consist of the highest number of deepest EREs (e.g., top 0.01% EREs > 15.50 km). EREs with MH40 show similar characteristics but the corresponding altitude is > 15.875 km (Figure 3). The top 0.01% deepest EREs based on MH40 are mostly found over land-dominated areas, such as South Asia, central Africa, central South America, and the south of United States of America. The EREs with higher 40 dBZ echoes are also found over the mid latitude and subtropical areas, such as northern Europe, Siberian Russia, and central Canada. It clearly indicates that even if the oceanic areas and mid latitude have largest EREs, they are not deep enough. Figure 4 shows the global distribution of intense EREs. Again, up to top 0.1% intense rainy events (>130.06 mm h^{-1}) follow the rainfall climatology, but the top 0.01% (>299.62 mm h^{-1}) intense rainy events show the different characteristics compared to the largest and deepest EREs. For example, both land and oceanic areas consist of the top 0.01% intense rain events, and most of the intense EREs occur over central South America, central Africa, South East South Asia, Maritime Continent, coastal regimes, central Pacific, southern Atlantic, and South America.

Spatial distribution of EREs shows the land-ocean contrast as well as the regional characteristics. The largest and deepest EREs (top 0.01%) occurrences show the land and ocean contrast, as mostly subtropical oceans and tropical land areas, consist of the largest and deepest EREs, respectively. However, intense EREs occur both over the tropical land and oceanic areas (Figure 4(d)). It clearly indicates that largest EREs do not correspond to the deepest or intense EREs over land (quantified later), and over land, the intense EREs are deeper, compared to the ocean where shallower EREs may be an intense one as shown in

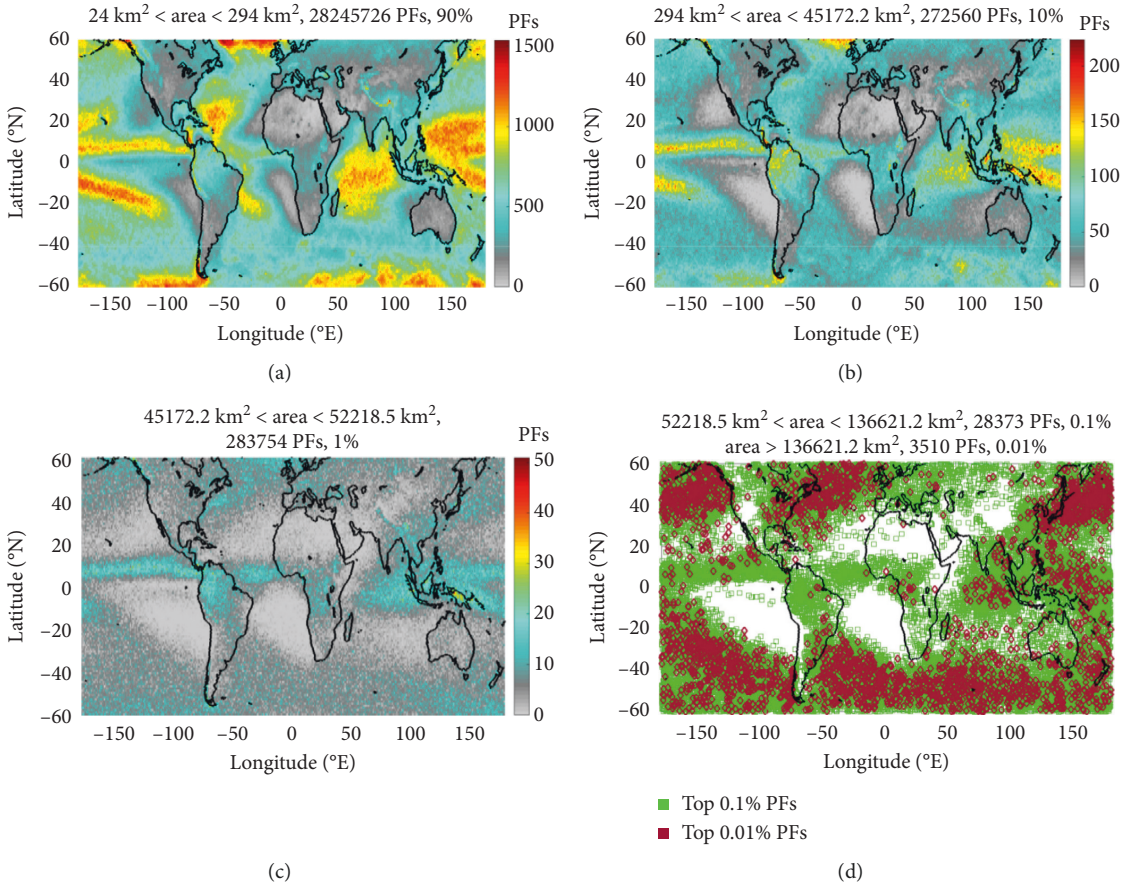

Figure 1: Spatial distribution of largest (in size) extreme rainfall events over the globe. (a–c) The distribution of largest extreme rainfall events in each $1^\circ \times 1^\circ$ box; (d) the actual geographical locations of largest extreme rainfall events. Color bar in (a)–(c) shows the number of extreme rainfall events. (d) The green color refers to the top 0.1% PFs, whereas magenta refers to the top 0.01% largest PFs.

[4, 34, 35]. In the next section, we will discuss the importance of these EREs in world precipitation.

3.2. The Fraction of the Global Precipitation from Extreme Rainfall Events. EREs are very important as they contribute to most of the global precipitation [33]. Figure 5 shows the fraction of global precipitation in each 1° latitude belt for the EREs based on MH20. Here, two important features are observed. First, tropical areas have a higher number of deeper EREs, which contribute to a higher fraction of rainfall in world precipitation, whereas, beyond 25°, a higher fraction of precipitation comes from shallower EREs. The deeper EREs (top 1% > 15.50 km) are less but contribute to the highest fraction of precipitation over the tropics, whereas over the mid latitude, most of the precipitation comes from the EREs less than 7.5 km altitude and mostly belongs to the top 10% of the deepest EREs. These findings are consistent with the past studies [33, 48, 49]. The higher fraction from shallow precipitation over the southern hemisphere is due to the large regions of weak and shallow rainfall over the area (e.g., stratocumulus regions west coast of Chile and Africa). A clear difference is observed between the northern and southern hemisphere, and each latitude in the northern hemisphere has higher deeper EREs compared to the corresponding latitude in the southern hemisphere.

Table 3 provides a brief information of the fraction of the global precipitation contributed by different types of EREs. The top 1% largest EREs contribute more than 36% of the total global precipitation, whereas the corresponding contribution for top 1% deepest EREs based on MH20 (>10.625 km) and MH40 (>9.5 km) are only 14.3 and 4.5%. The land and ocean contrast are also visible as land-based deepest EREs contribute to higher global precipitation compared to oceanic based deepest EREs; however, the largest EREs show the opposite characteristics. The top 0.01% largest EREs contribute to more than ~8.0% rainfall over the oceans, compared to the land where the top 0.01% largest EREs only contribute to ~2.6% rainfall. Although the deepest EREs based on MH40 contribute to a higher fraction of rainfall (3.1%) over land-dominated areas compared to oceanic areas (1.8%).

3.3. Regional Distribution of Extreme Rainfall Events over SA and SAsia during Different Seasons. We selected two monsoon domains/zone, namely, SAsia and SA, during JJAS and DJFM months to compare the characteristics of EREs. Figure 6 shows the geographical locations of top 10% (blue),

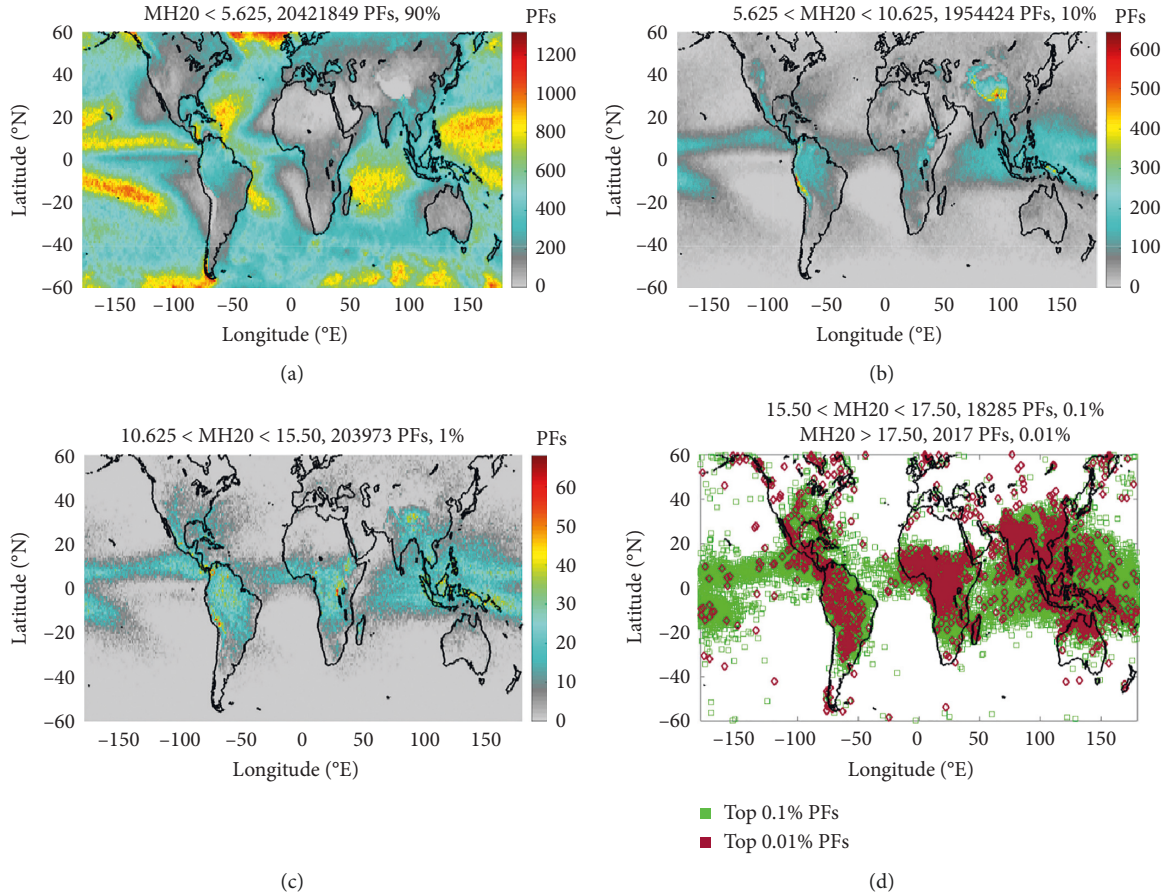

Figure 2: Spatial distribution of deepest (in depth, km) extreme rainfall events over the globe based in the maximum height of 20 dBZ. (a–c) The distribution of deepest extreme rainfall events in each $1^{\circ} \times 1^{\circ}$ box; (d) the actual geographical locations of deepest extreme rainfall events. Color bar in (a)–(c) shows the number of extreme rainfall events. (d) The green color refers to the top 0.1% deepest PFs, whereas magenta refers to the top 0.01% deepest PFs.

1% (green), 0.1% (violet) and 0.01% (black) EREs based on the various criteria (Table 2) over SA and SAsia. Table 4 shows the thresholds used in the present study for DJFM and JJAS seasons. During DJFM months, the largest EREs (top 0.1% largest PFs, 53320 km^2) occur over central SA, southern Chile, south of the Atlantic Ocean, and Amazon basin [32, 36]. The largest EREs over the Amazon is linked to low-level jets (LLJ), which carry the moist air from the Amazon and produces the heavy precipitation at the eastern flank of the Andes [50]. The deepest EREs show the different characteristics compared to the largest EREs, and the regional differences are much higher. For example, the deepest EREs (top 0.1% EREs>16.25 km) mostly occur over central SA including the north SA, La Plata basin, Sierra de Cordoba, central Andes, and southern Chile. The higher number of deepest EREs over/near the Andes reflects the orographic-induced convection [32, 36]. The Atlantic Ocean does not consist of a single ERE categorized by the top 0.01% deepest EREs and is consistent with the weak convection over the Atlantic [23, 28, 29, 32]. The deepest EREs based on MH40 show the most interesting characteristics, as both Atlantic Ocean and Pacific Ocean do not consist of a single ERE belong to the top 1% deepest EREs, and the deepest EREs mostly occur over the land area (top 0.01%; >14.0 km). The spatial distribution of the largest volumetric rainfall EREs shows that most of the largest EREs are located near the Brazilian highlands and the Atlantic Ocean and nearly coincides with the locations of the largest EREs. The intense EREs (top 1%) reveal the importance of the role of orography in intense rainfall events, as during DJFM seasons, the areas near and at the Andes have the higher number of intense rainfall events (top 1% EREs>44 mm h^{-1}), along with the La Plata basin and Brazilian Highlands. Overall, northern SA has higher intense EREs compared to southern SA.

Figure 6(b) shows the geographical locations of EREs over SAsia during JJAS months. The spatial distribution shows that the Bay of Bengal (BOB) and the head of the Bay have a higher number of the largest EREs (top 0.1% largest EREs; 53000 km^2). These findings are consistent with the past studies that the BOB has the most organized larger convective systems [23, 33, 35, 37]. The Western Ghats (WG), Arabian Sea, and tropical Indian Ocean also consist of fewer largest EREs (>53000 km^2). The deepest EREs based on MH20 show different characteristics, as the IGP and WG have the higher number of deeper EREs (top 0.1%; >11.5 km). Myanmar and Karakoram hills also consist of

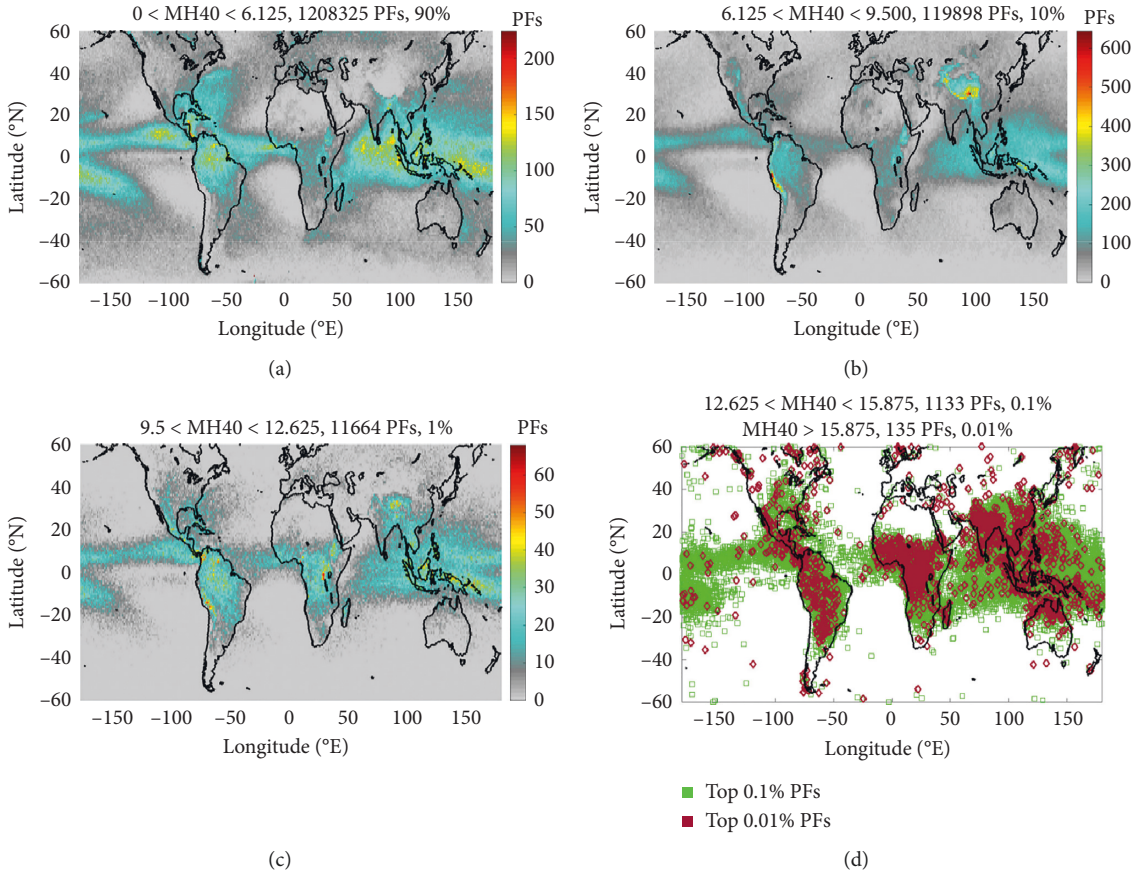

Figure 3: Spatial distribution of deepest (in depth, km) extreme rainfall events over the globe based in the maximum height of 40 dBZ. (a–c) The distribution of deepest extreme rainfall events in each $1^{\circ} \times 1^{\circ}$ box; (d) the actual geographical locations of deepest extreme rainfall events. Color bar in (a)–(c) shows the number of extreme rainfall events. (d) The green color refers to the top 0.1% deepest PFs, whereas magenta refers to the top 0.01% deepest extreme rainfall events.

fewer deeper EREs [26]. The deepest EREs based on MH40 show an interesting characteristic as they (top 0.1% EREs > 13.5 km) are located mostly over the land areas, such as over the Western Himalaya Foothills (WHF), IGP, and central India and reflect the land and ocean differences. The WG and Arabian Sea have the shallowest EREs (<5.0 km) during the monsoon season [28, 31]. The largest EREs based on the amount of volumetric rainfall follow the largest EREs distribution, and most of the largest EREs correspond to the higher volumetric rainfall, especially over the BOB and Arabian Sea. The land-dominated areas have fewer largest EREs, which contribute to higher volumetric rainfall compared to oceanic areas. The most intense EREs show the interesting characteristics, and both land and oceanic areas consist of intense EREs. Areas over the head of the Bay, BOB, Arabian Sea, Karakoram hills, and WG have the highest intense EREs (top 0.1% intense EREs>125 mm h^{-1}), but they do not coincide with the largest EREs, except over the BOB. During JJAS months, the topographic areas such as the IGP and WHF consist of fewer intense EREs (top 0.1% > 133 mm h^{-1}) and reflect the mountain's role [51]. The WG and the Arabian Sea also have few large and intense EREs [26].

The spatial distribution of the deepest, largest, and intense EREs indicates the effect of specific geographical features, climatological wind pattern, humidity, topography, and role of cloud condensation nuclei (CCN). It has been long known that the wind shear and upslope motion at the wind-ward and lee side of the mountain can alter the microphysical processes and lead to a change in rainfall characteristics [51]. The smaller number of the largest and deepest EREs at west of the Andes and south most (including Pacific Ocean) of the Andes are related to South-East Subtropical Anticyclone (SPSA) in the South Pacific basin. The SPSA generates the stable and arid condition at the western slope of the Andes [52], which does not allow the deep convection and does not allow the moisture to rise above 900 hPa. South American LLJ transports the moisture along the eastern edge of the Andes from the tropical regions to the subtropical part of the continent (850 level), and it triggers the deep and intense convection mostly at the eastern flank of the Andes [32]. The deepest convections over the WHF and Sierra de Cordoba along with La Plata basin are due to their specific geographical feature and wind pattern. Median et al. [53] and Romatscheke and Houze [32] explained that instability generated within the moist boundary layer in two areas is not easily released. The only way to produce the deep and intense convection over these areas is the orographic motion. Whenever an unstable and orographically induced flow moves along the steep slope and reaches up to the saturation level, it

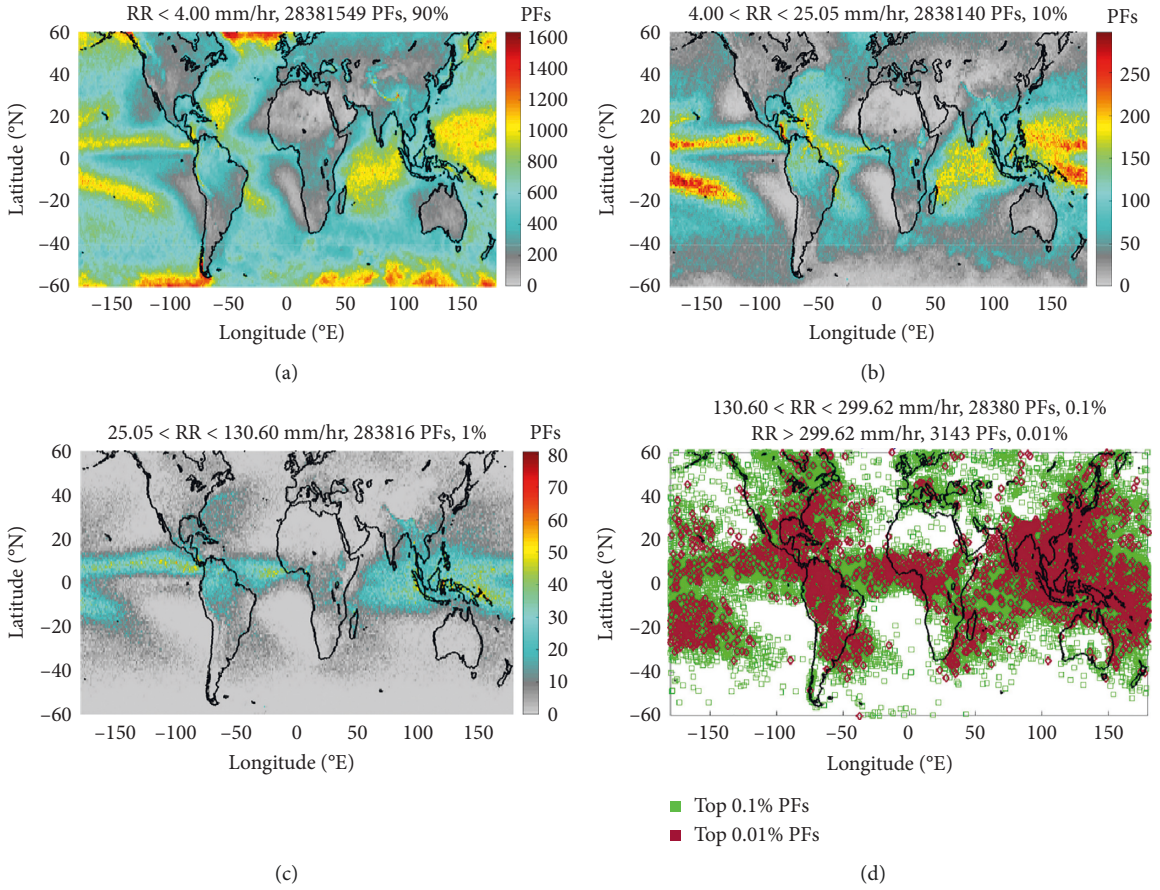

Figure 4: Spatial distribution of intense extreme rainfall events (in mm h^{-1}) over the globe based on the rainfall rate. (a–c) The distribution of intense extreme rainfall events in each $1^{\circ} \times 1^{\circ}$ box; (d) the actual geographical locations of intense extreme rainfall events. Color bar in (a)–(c) shows the number of extreme rainfall events. (d) The green color refers to the top 0.1% intense extreme rainfall events, whereas magenta refers to the top 0.01% intense extreme rainfall events.

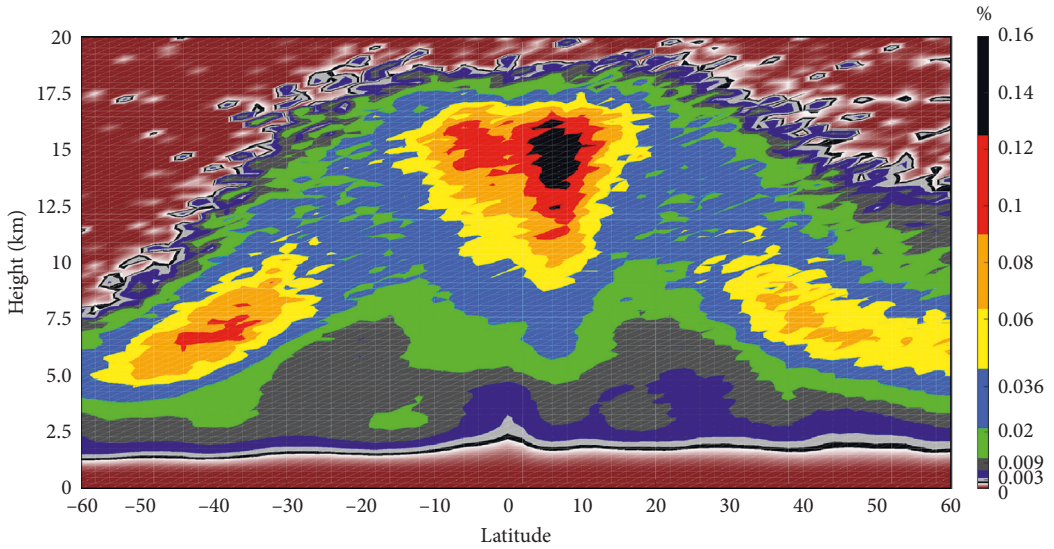

Figure 5: Contribution to global precipitation from extreme rainfall events of different maximum heights of the 20 dBZ echo. Here, the statistics are computed in 1° latitude bins.

Table 3: Contribution to global precipitation by largest, deepest, and intense PFs.

PFs	Intensity	Top 10%	Top 1%	Top 0.1%	Top 0.01%
Largest (area)	Total	96.4	80.7	36.1	7.1
	Ocean	96.2	82.2	40.5	8.6
	Land	97.2	76.3	23.0	2.6
Maximum height of 20 dBZ (MH20)	Total	90.6	53.1	15.4	1.8
	Ocean	89.1	51.5	14.3	1.4
	Land	94.9	57.8	18.8	3.1
Maximum height of 40 dBZ (MH40)	Total	86.7	53.3	9.5	1.2
	Ocean	86.3	49.8	4.5	0.4
	Land	87.6	63.9	24.8	4.0

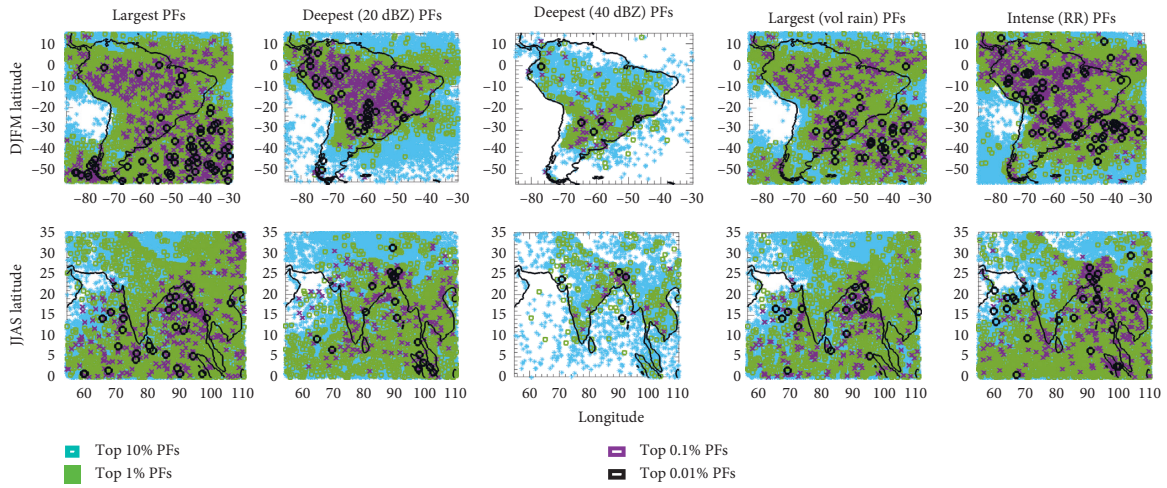

Figure 6: Spatial distribution of largest, deepest, and intense extreme rainfall events over South America (upper rows) and South Asia (bottom rows) during December to March (DJFM) and June to September (JJAS) months, respectively. The different seasons are mentioned in the *Y*-axis. The first, second, third, fourth, and fifth columns are for the largest extreme rainfall events based on area, deepest extreme rainfall events based on maximum height of 20 dBZ, deepest extreme rainfall events based on maximum height of 40 dBZ, largest extreme rainfall events based on the quantity of volumetric rainfall, and intense extreme rainfall events based on the rain rate.

Table 4: Fraction contribution in seasonal and regional precipitations by extreme events based on the area over the land and ocean.

Season and number of PFs		Volumetric rainfall contribution (in %)				Thresholds			
		Top 10%	Top 1%	Top 0.1%	Top 0.01%	Top 10%	Top 1%	Top 0.1%	Top 0.01%
For the largest PFs (km^2)									
DJFM/land	290919	94.97	67.95	22.07	3.68	540.1000	8.9362$e+03$	5.4077$e+04$	1.0730$e+05$
DJFM/ocean	388683	96.74	84.06	36.18	8.21	270.05	4.1735$e+03$	5.1749$e+04$	1.4738$e+05$
JJAS/ocean	253470	97.28	82.61	32.42	5.52	343.7000	6.0639$e+03$	5.9044$e+04$	1.2510$e+05$
JJAS/land	235396	94.32	64.93	21.91	4.10	540.1000	8.1997$e+03$	4.8941$e+04$	1.0320$e+05$
Maximum height of 20 dBZ (MH20)									
DJFM/land	237542	84.54	28.50	4.64	0.62	8.500	14.500	16.875	18.250
DJFM/ocean	286051	91.16	53.12	12.82	2.60	5.250	9.250	13.750	16.125
JJAS/ocean	191865	94.69	57.98	12.49	1.57	7.00	12.250	16.000	18.250
JJAS/land	185994	81.03	28.30	4.38	0.38	9.375	15.000	17.565	19.985
Maximum height of 40 dBZ (MH40)									
DJFM/land	36953	38.8	8.36	1.75	0.20	7.125	10.750	14.250	16.450
DJFM/ocean	17490	52.96	10.44	2.34	0.14	5.125	7.500	11.375	16.125
JJAS/ocean	26522	64.9	14.65	2.79	0.18	5.875	8.250	11.2475	16.500
JJAS/land	28598	54.62	39.42	4.93	1.01	8.000	11.250	14.475	16.625
Intense rainfall events (mm/hr)									
DJFM/land	290919	88.26	50.63	10.20	1.95	7.37	59.35	216.30	299.90
DJFM/ocean	388683	94.45	69.50	25.10	5.01	4.74	30.75	125.62	299.61
JJAS/ocean	253470	96.23	77.24	24.31	3.22	6.67	55.12	206.04	299.96
JJAS/land	235396	87.33	45.94	10.06	1.42	7.72	73.43	299.11	299.97

causes the instability to release and produces the deep and intense convection. The west side/coast of SAsia has lower CCN concentration [54], which increases the warm rain frequency that allows a few hydrometeors to go into the deep atmosphere [55], and at the same time, the higher CCN concentration over the land-dominated areas specially over the central and IGP delays the precipitation processes [55, 56] and is responsible for the deep and intense convection. The Arabian Sea has less deeper EREs during JJAS months because of Giant CCNs, which initiate the early warm rain processes and do not allow the deep convection [55]. The weak vertical velocity over the oceanic area is not able to lift the hydrometeors at a higher altitude and responsible for less cloud depth or cloud tops over the oceanic areas.

Figure 6 shows that the largest EREs are not the deepest ones, and the geographical location of EREs based on different parameters show the weak linkage between the largest, deepest, and intense EREs. These are quantified in detail in the next section. This reveals the atmospheric conditions which produce intense EREs are different from those produce the largest and deepest EREs. The regional and seasonal differences in EREs are related to different atmospheric conditions (e.g., [57]). This situation is well observed in [26, 27], where they showed the geographical features, and specific locations could produce very deep convection although their frequency could be less. For example, Zipser et al. [23] explained that the Amazon has a higher number of EREs in December–February (DJF), but the intense and deepest convection occurs mostly in the post-monsoon season [48]. The highest land and ocean contrasts are visible in the deepest EREs, as the Pacific, Atlantic, BOB, and Arabian Sea do not have a higher number of the deepest EREs. These EREs are not crossing 12 km altitude, whereas EREs of the nearby land areas are higher than 17 km. Both SA and SAsia show the mountain's (topographic) role in the generation of intense EREs, and most of the intense EREs occur near the topographic areas [51]. Land vs ocean contrast in the deepest EREs could be related to the weaker vertical velocity over the oceanic areas, which are not able to carry the hydrometeors at a higher altitude.

3.4. Linage between Extreme Events Based on Various Parameters. Hamada et al. [4] observed a weak linkage between the extreme convective and rainfall events, e.g., a very small fraction of extreme convective events produce the higher rainfall over the tropics and subtropics. The correlation was stronger over the tropical oceans (~50%) compared to land areas (~10%). A similar characteristic is observed in [33] where geographical locations of the largest and deepest EREs do not match. Here, we examined the linkage between the top 10% EREs based on various parameters. For example, for the largest EREs, parameters such as MH20, MH40, volumetric rainfall area, and RR are estimated. In Figure 7, the first row shows the CDF of MH20, MH40, volumetric rainfall area, and RR for the top 10% largest EREs (see the figure comment for more details). The second row shows the CDF of the area, MH20, volumetric rainfall area, and RR for the top 10% deepest EREs based on the MH40, whereas the third row shows the CDF of area, MH20, MH40, and volumetric rainfall area for top 10% intense EREs based on the RR.

For the largest top 10% EREs (Figure 7(a1)), the seasonal and regional differences are apparent. For example, SAsia has a higher frequency of the deepest EREs (MH20 is higher) compared to SA for the largest EREs. For 50% of the largest top 10% EREs during JJAS months, MH20 is higher than 7 km altitude, whereas the corresponding altitude for SA is ~5.5 km (Figure 7(a1)). EREs with MH20 higher than 8.5 km altitude correspond to only the top 10% deepest EREs, and so within the largest 10% EREs, ~20% of them correspond to the top 10% deepest EREs over SAsia (~7 km), whereas over SA ~30% largest EREs corresponds to the top 10% deepest EREs. Also, for ~50% of the largest top 10% EREs, MH40 are crossing the 12 km altitude, whereas the corresponding percentage and altitude over SA is 70% and ~8–9 km (Figure 7(a2)). It indicates that there is a higher probability that the largest EREs could be the deepest during JJAS months compared to DJFM months. Volumetric rainfall area shows the opposite characteristics, and the top 10% largest EREs over SAsia do not provide the much volumetric rainfall amount compared to SA. This indicates that small EREs are also able to contribute to significant rainfall over SAsia during JJAS months. The RR is also higher during JJAS seasons over SAsia compared to SA for the top 10% largest EREs. More than ~50% of the top 10% largest EREs have a RR higher than 75 mm h^{-1} during JJAS months, whereas the corresponding RR is only 50 mm h^{-1} during DJFM over SA (Figure 7(a4)). Over both the areas, only 35–45% of the largest EREs have a RR that is higher than the top 1% intense RR (Table 4) which indicates that very few of the largest EREs correspond to intense rainy events (~63 and ~50 mm h^{-1} during JJAS and DJFM over SAsia and SA).

MH40 also shows the regional and seasonal differences for the top 10% deepest EREs, and JJAS months have higher deeper EREs over SAsia. For the ~50% of the top 10% deepest EREs, MH20 is higher than 8.5 km (top 10% deepest EREs) over SAsia, whereas over SA, for the ~40% deepest EREs, MH20 corresponds to the top 10% deepest EREs (7 km, Table 4). Area for the top 10% deepest EREs does not show much seasonal differences (Figure 7(b2)). Although in small differences, SA has a higher frequency of the deepest EREs, which can produce a higher amount of volumetric rainfall. The deepest EREs have a higher chance to be intense during DJFM months and more than ~40% of the deepest EREs have a RR higher than 50 mm h^{-1}, which corresponds to the top 1% intense EREs. Importantly, thresholds over SAsia (63 mm h^{-1} for top 1%) is higher compared to SA (50 mm h^{-1} for top 1%), but there is a higher probability (~45%) for them to be quantified as a part of the top 1% intense rainy events over SAsia for the deepest EREs. For the top 10% intense rainfall EREs, MH20 and MH40 show the least regional and seasonal differences (Figures 7(c1) and 7(c2)), and EREs over SAsia are deeper when compared to SA. The area and volumetric rainfall area do not show much regional differences for intense EREs.

Figure 7 shows that the linkage between the EREs is higher over SAsia compared to SA, and there is a higher

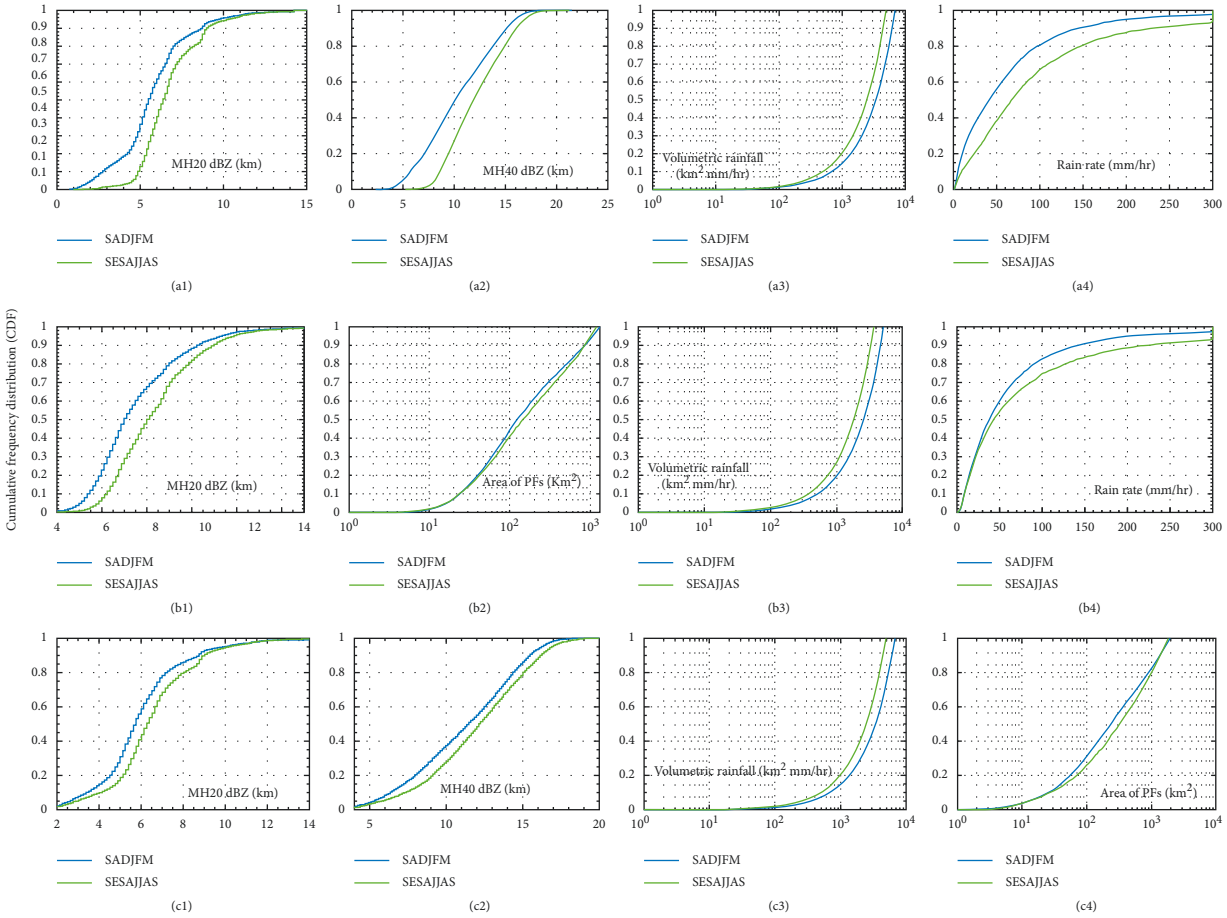

Figure 7: The cumulative frequency distribution (CDF) of area, maximum height of 20 dBZ, maximum height of 40 dBZ, volumetric rainfall, and rain rate for each type of extreme rainfall events. As an example, in the first row, the MH20, MH40, volumetric rainfall area, and rain rate are calculated for the top 10% largest PFs.

probability that the largest EREs belong to the deepest and intense EREs over SAsia, compared to SA. It is very important to see that thresholds for EREs area, MH20, MH40, and rain rate over SA are higher/lower compared to SAsia, depending on the land and ocean. The land areas have higher deepest EREs over SAsia (>14.75 for top 0.1% EREs) compared to SA (>12.75 for top 0.1% EREs). The opposite characteristics are observed over the oceans. The least regional and seasonal differences are observed in intense EREs, it could be the orthographically induced convection produced them [51].

3.5. Fraction of the Global Precipitation from Extreme Rainfall Events during JJAS and DJFM Months. Figure 8 shows the fraction of precipitation from the deepest EREs based on MH20 at different latitudes in 1° latitude belts over SA and SAsia (Figures 8(a) and 8(b)) during DJFM and JJAS month. During both the seasons, the deepest EREs based on MH20 are crossing 12.5–17 km over the tropics and contribute to the higher fraction of seasonal and regional precipitation, although they are relatively rare (belongs to only top 0.1 deepest EREs, Table 4). MH20 higher than 12 km could be related to Cumulonimbus clouds [26, 27, 58] and is responsible for the large precipitation contribution. At the mid and higher latitude, shallower EREs are contributing to the higher amounts of rainfall [31], as in Figure 5. In a small seasonal difference, SA (during DJFM month) has a higher fraction of rainfall from little deeper EREs (14 km < MH20 < 17.5 km) compared to SAsia, where the maximum fraction on rainfall comes from EREs with MH20 lies between 11 and 16.5 km altitude. The northern hemisphere has higher precipitation contribution by deeper EREs compared to the southern hemisphere and possibly the higher land areas in the northern hemisphere are responsible for them. There are a higher number of shallower EREs, but their precipitation contribution is not as significant, which is consistent with past studies (e.g., [26, 33, 52]). Satellite-based observations show that during the DJFM season, the Andes Mountain along with the surface wind flow affects the distribution of the precipitating cloud systems [59–62], and wind shear could also affect the microphysical processes and leads the different cloud tops with different rainfall intensities [63].

Figure 9 shows the fraction of precipitation from the deepest EREs based on MH40 at different latitudes in 1° latitude belts over SA and SAsia (Figures 9(a) and 9(b))

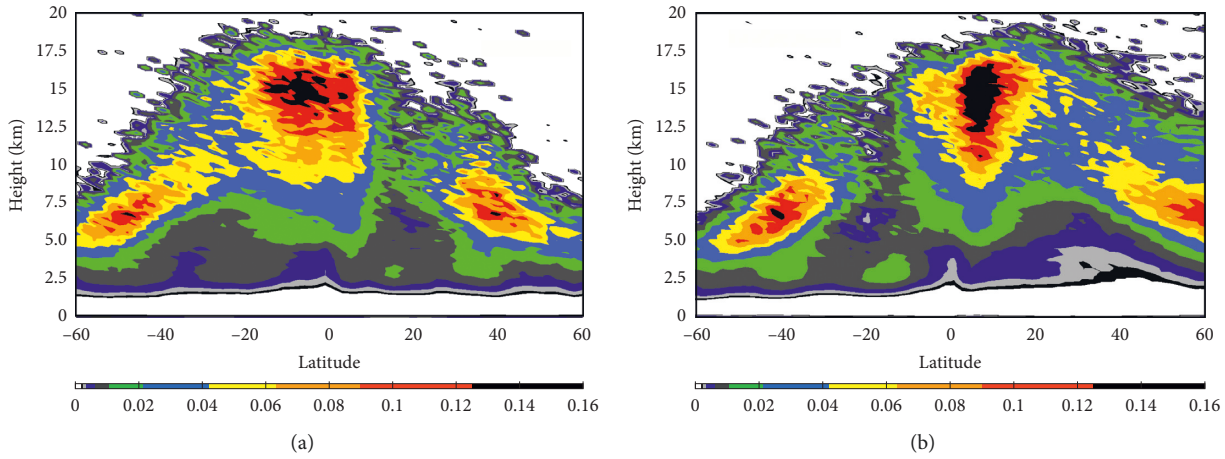

FIGURE 8: Contributions to global precipitation from extreme rainfall events of different maximum heights of the 20 dBZ echo. In all cases, the statistics are computed in 1° latitude bins. Total values add up to 100%. (a) DJFM; (b) JJAS.

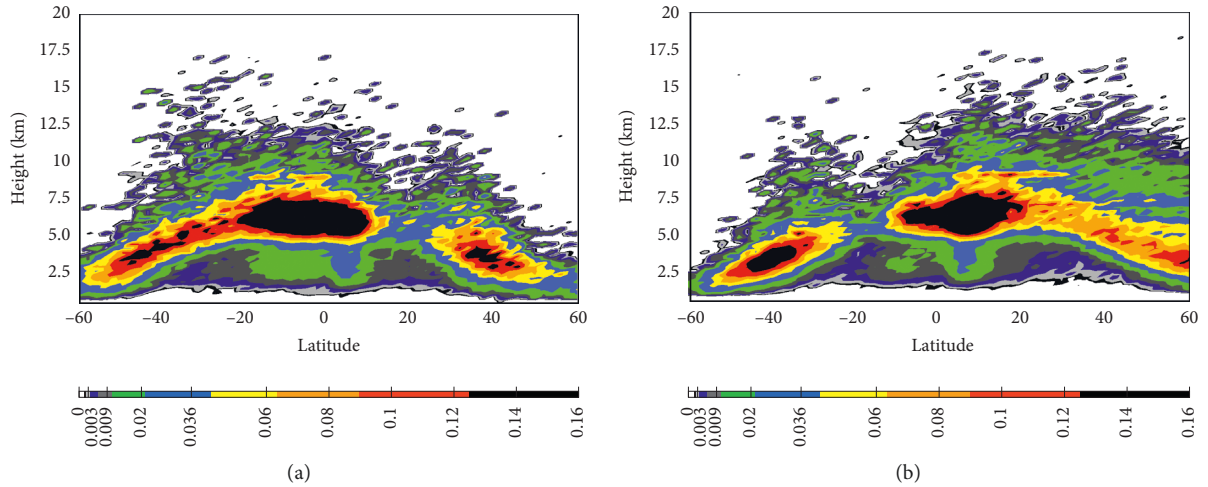

FIGURE 9: Contributions to global precipitation from PFs of different maximum heights of the 40 dBZ echo. In all cases, the statistics are computed in 1° latitude bins. Total values add up to 100%. (a) DJFM; (b) JJAS.

during DJFM and JJAS months, respectively. The regional and seasonal differences are higher here; and a higher fraction of precipitation comes from deeper EREs (5 km < MH40 < 10 km) during DJFM months. JJAS also shows the similar trends, but at the southern latitudes, it also shows a maxima from the sallower clouds. At mid and higher latitudes, shallower EREs contribute to a higher fraction of rainfall, as in Figure 6. Figure 10 shows the contributions to seasonal and regional precipitations from the deepest EREs based on MH40 at different latitudes in 1° latitude belts over SA and SAsia for land and ocean separately. Land and ocean contrasts are observed, and land areas have a higher fraction of rainfall from deeper EREs, compared to oceanic areas, during both the seasons. The land differences are higher in both the seasons compared to oceanic areas, as oceanic areas show similar characteristics, and the maximum amount of the rainfall comes from the EREs, with MH40 lying between 4 and 6 km, within tropical areas. Interestingly, JJAS shows the two bands over the land-dominated areas, namely, at 7 and 9 km altitude.

Table 4 shows brief information about the fraction of global precipitation by the EREs over land and oceanic areas during JJAS and DJFM months. For example, the top 0.1% largest EREs contribute more than 22% of the regional precipitation over land during DJFM months, whereas during JJAS month, the corresponding number is higher than 32%. During both the seasons largest EREs contribute to higher volumetric rainfall compared to that over the land. The deepest EREs also show the regional and seasonal differences, as the top 0.1% deepest EREs based on MH20 (MH40) contribute nearly ~12.4% ((~2.8%) over ocean) and ~4.3% ((4.9%) over land) of regional precipitation during JJAS months, whereas the corresponding contribution during DJFM months is only ~4.6% ((~12.8%) over ocean) and ~4.6% ((1.79%) over land). For all the parameters, the land and oceanic differences are evident and tabulated in Table 4.

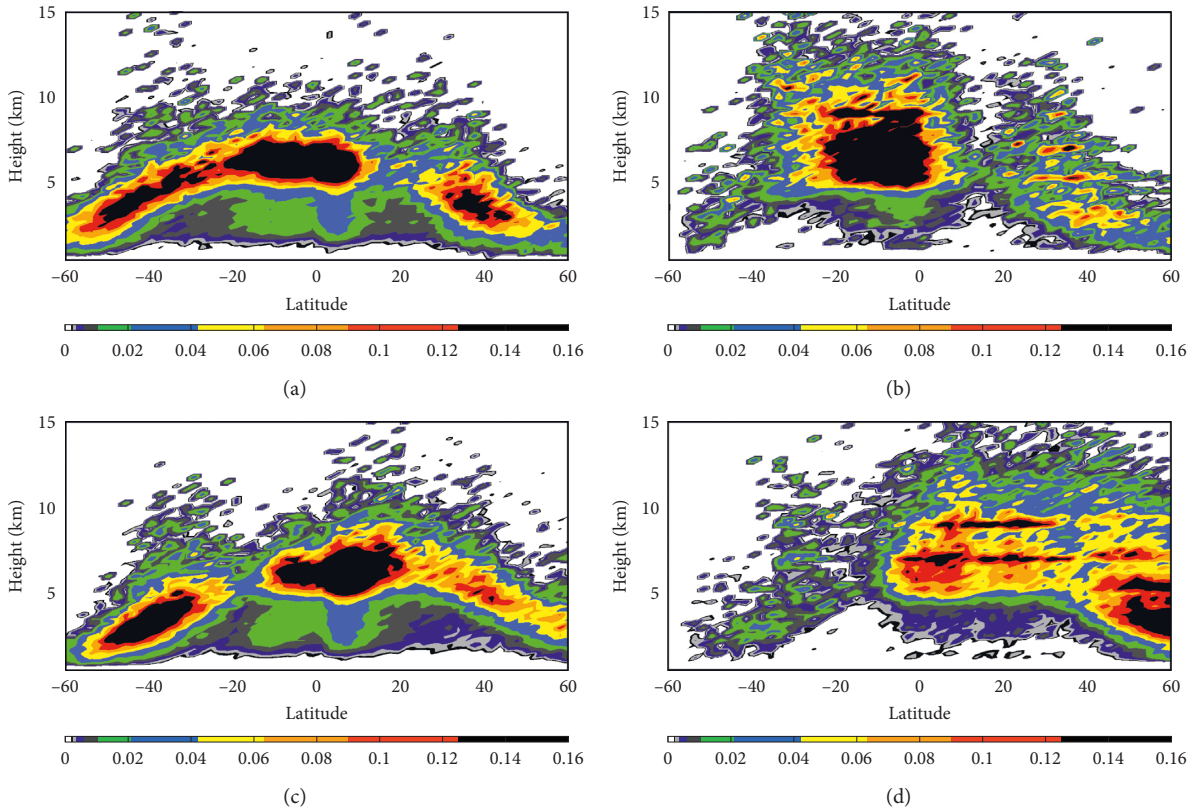

Figure 10: Contributions to global precipitation from extreme rainfall events of different maximum heights of the 40 dBZ echo over the land and ocean. In all cases, the statistics are computed in 1° latitude bins. (a) DJFM-ocean; (b) DJFM-land; (c) JJAS-ocean; (d) JJAS-land.

4. Conclusions

PFs data based on GPM satellite are used to explore the spatial distribution of extreme rainfall events/PFs on a global scale as well as the regional scale. We also selected the two main monsoon zones, namely, over South Asia and South America during different seasons to explore the spatial distribution of extreme rainfall events. The main conclusions from the present study are the following:

(1) The spatial distribution shows a large regional variation in EREs based on the area, depth, and rain rate. The spatial distribution of the largest and deepest EREs (top 0.01% EREs) shows the land and ocean differences. Subtropical oceans and tropical land-dominated areas consist of the largest and deepest EREs, respectively. It is clear that the largest EREs do not correspond to the deepest EREs. However, the intense EREs occur both over the tropical land and oceanic areas. Geographical locations of the deepest and intense EREs over the land-dominated area indicate that the intense EREs are deeper ones compared to the ocean, where the shallower EREs could also be an intense one.

(2) The top 1% largest EREs contribute to ~80.7% of Earth's precipitation, whereas the corresponding % for the deepest EREs is only 53%. Tropical areas have a higher number of deeper EREs contributing to a higher fraction of rainfall in world precipitation, whereas, beyond 25°, the higher fraction of precipitation comes from shallower EREs. The deeper extreme rainfall events (top 1% > 15.50 km) are less but contribute to the highest fraction of precipitation over the tropics, whereas over the mid latitude, most of the precipitation comes from the EREs less than 7.5 km altitude and mostly belongs to the top 10% of the deepest extreme rainfall events.

(3) Geographical locations of the largest, deepest, and intense EREs over South Asia are regions dependent. The Bay of Bengal along with the Arabian Sea and Equatorial Indian Ocean consists of the largest EREs, whereas the deepest EREs mostly occur over the land-dominated areas. The Western Himalaya foothills, Western Ghats, and Indo-Gangetic plain consist of the deepest EREs during Indian summer monsoon seasons. South America also shows similar characteristics and the Atlantic Ocean consists of the largest EREs followed by the Amazon and southern Chile. The deepest extreme rainfall events show different characteristics, as the Amazon also has the deepest EREs along with east side of the Andes. Subtropical South America including Sierra de Cordoba and La Plata basin consists of the largest, deepest, and extreme EREs during DJFM.

(4) Extreme rainfall events are highly linked over South Asia compared to South America based on different thresholds. For example, the top 10% largest extreme

rainfall events have a higher probability to be the part of the top 10% deepest and intense extreme rainfall events. Also, the deeper and intense rainy extreme events are highly linked over South Asia compared to South America.

(5) The seasonal and regional water budget reveals the regional characteristics, as the southern hemisphere has higher deeper extreme rainfall events, contributing to seasonal and regional precipitation budget. The tropical ocean has a higher number of shallower extreme rainfall events that contribute to higher water budget compared to land, where more precipitations occur due to deeper extreme rainfall events.

Data Availability

The data used to support the findings of this study are available from the corresponding author upon request.

Disclosure

The present study was performed under the project "MAGNET-IGP: strengthening the research line in physics and microphysics of the atmosphere" (agreement no. 010-2017-FONDECYT).

Conflicts of Interest

The authors declare that there are no conflicts of interest regarding the publication of this paper.

Acknowledgments

The authors would like to thank the CONCYTEC, Peru, for financial support and the Inter-American Institute for Cooperation on Agriculture (IICA) for administrative support.

Supplementary Materials

Supplementary Figure 1: the selection of largest PFs based on the area. (*Supplementary Materials*)

References

[1] C. Schumacher, R. A. Houze, and I. Kraucunas, "The tropical dynamical response to latent heating estimates derived from the TRMM Precipitation Radar," *Journal of the Atmospheric Sciences*, vol. 61, no. 12, pp. 1341–1358, 2004.

[2] R. A. Houze, "Mesoscale convective systems," *Reviews of Geophysics*, vol. 42, no. 4, article RG4003, 2004.

[3] R. Roca, J. Aublanc, P. Chambon, T. Fiolleau, and N. Viltard, "Robust observational quantification of the contribution of mesoscale convective systems to rainfall in the tropics," *Journal of Climate*, vol. 27, no. 13, pp. 4952–4958, 2014.

[4] A. Hamada, Y. N. Takayabu, C. Liu, and E. J. Zipser, "Weak linkage between the heaviest rainfall and tallest storms," *Nature Communication*, vol. 24, no. 6, p. 7213, 2015.

[5] R. A. Houze, K. L. Rasmussen, S. Medina, S. R. Brodzik, and U. Romatschke, "Anomalous atmospheric events leading to the summer 2010 floods in Pakistan," *Bulletin of the American Meteorological Society*, vol. 92, no. 3, pp. 291–298, 2011.

[6] R. A. Houze Jr and A. K. Betts, "Convection in GATE," *Reviews of Geophysics*, vol. 19, no. 4, pp. 541–576, 1981.

[7] R. A. Houze, "Cloud clusters and large-scale vertical motions in the tropics," *Journal of the Meteorological Society of Japan*, vol. 60, pp. 396–410, 1982.

[8] J. L. Redelsperger, *The mesoscale organization of deep convection The Physics and Parameterization of Moist Atmospheric Convection*, NATO ASI Series, R. K. Smith, Ed., vol. 505, Springer, Berlin, Germany, 1997.

[9] R. A. Houze, K. L. Rasmussen, M. D. Zuluaga, and S. R. Brodzik, "The variable nature of convection in the tropics and subtropics: a legacy of 16 years of the Tropical Rainfall Measuring Mission (TRMM) satellite," *Reviews of Geophysics*, vol. 53, no. 3, pp. 994–1021, 2015.

[10] R. W. Spencer and D. A. Santek, "Measuring the global distribution of intense convection over land with passive microwave radiometry," *Journal of Climate and Applied Meteorology*, vol. 24, no. 8, pp. 860–864, 1985.

[11] R. W. Spencer, H. M. Goodman, and R. E. Hood, "Precipitation retrieval over land and ocean with the SSM/I: identification and characteristics of the scattering signal," *Journal of Atmospheric and Oceanic Technology*, vol. 6, no. 2, pp. 254–273, 1989.

[12] K. I. Mohr and E. J. Zipser, "Defining mesoscale convective systems by their 85-GHz ice-scattering signatures," *Bulletin of the American Meteorological Society*, vol. 77, no. 6, pp. 1179–1189, 1996.

[13] R. E. Orville and R. W. Henderson, "Global distribution of midnight lightning: September 1977 to August 1978," *Monthly Weather Review*, vol. 114, no. 12, pp. 2640–2653, 1986.

[14] C. Kummerow, W. Barnes, T. Kozu, J. Shiue, and J. Simpson, "The tropical rainfall measuring mission (TRMM) sensor package," *Journal of Atmospheric and Oceanic Technology*, vol. 15, no. 3, pp. 809–817, 1998.

[15] S. W. Nesbitt, R. Cifelli, and S. A. Rutledge, "Storm morphology and rainfall characteristics of TRMM Precipitation Features," *Monthly Weather Review*, vol. 134, no. 10, pp. 2702–2721, 2006.

[16] C. Liu, E. J. Zipser, D. J. Cecil, S. W. Nesbitt, and S. Sherwood, "A cloud and precipitation feature database from nine years of TRMM observations," *Journal of Applied Meteorology and Climatology*, vol. 47, no. 10, pp. 2712–2728, 2008.

[17] S. W. Nesbitt, E. J. Zipser, and D. J. Cecil, "A census of precipitation features in the tropics using TRMM: radar, ice scattering, and lightning observations," *Journal of Climate*, vol. 13, no. 23, pp. 4087–4106, 2000.

[18] Y. N. Takayabu, "Spectral representation of rain profiles and diurnal variations observed with TRMM PR over the equatorial area," *Geophysical Research Letters*, vol. 29, pp. 1–4, 2002.

[19] S. Kumar, "Three dimensional characteristics of precipitating cloud systems observed during Indian summer monsoon," *Advances in Space Research*, vol. 58, no. 6, pp. 1017–1032, 2016.

[20] D. J. Cecil, S. J. Goodman, D. J. Boccippio, E. J. Zipser, and S. W. Nesbitt, "Three years of TRMM precipitation features. Part I: radar, radiometric, and lightning characteristics," *Monthly Weather Review*, vol. 133, no. 3, pp. 543–566, 2005.

[21] H. Masunaga, T. S. L'Ecuyer, and C. D. Kummerow, "Variability in the characteristics of precipitation systems in the

tropical pacific. Part I: spatial structure," *Journal of Climate*, vol. 18, no. 6, pp. 823–840, 2005.

[22] C. Liu and E. Zipser, "Global distribution of convection penetrating the tropical tropopause," *Journal of Geophysical Research*, vol. 110, article D23210, 2005.

[23] E. J. Zipser, D. J. Cecil, C. Liu, S. W. Nesbitt, and D. P. Yorty, "Where are the most intense thunderstorms on Earth?," *Bulletin of the American Meteorological Society*, vol. 87, no. 8, pp. 1057–1072, 2006.

[24] R. A. Houze, D. C. Wilton, and B. F. Smull, "Monsoon convection in the Himalayan region as seen by the TRMM precipitation radar," *Quarterly Journal of the Royal Meteorological Society*, vol. 133, pp. 1389–1411, 2007.

[25] C. Liu and E. J. Zipser, ""Warm rain" in the tropics: seasonal and regional distributions based on 9 yr of TRMM data," *Journal of Climate*, vol. 22, no. 3, pp. 767–779, 2009.

[26] G. S. Bhat and S. Kumar, "Vertical structure of cumulonimbus towers and intense convective clouds over the South Asian region during the summer monsoon season," *Journal of Geophysical Research: Atmospheres*, vol. 120, no. 5, pp. 1710–1722, 2015.

[27] S. Kumar and G. S. Bhat, "Vertical profiles of radar reflectivity factor in intense convective clouds in the tropics," *Journal of Applied Meteorology and Climatology*, vol. 55, no. 5, pp. 1277–1286, 2016.

[28] S. Kumar and G. S. Bhat, "Vertical structure of orographic precipitating clouds observed over south Asia during summer monsoon season," *Journal of Earth System Science*, vol. 126, no. 8, p. 114, 2017.

[29] S. Kumar, "A 10-year climatology of vertical properties of most active convective clouds over the Indian regions using TRMM PR," *Theoretical and Applied Climatology*, vol. 127, no. 1-2, pp. 429–440, 2017.

[30] S. Kumar, "Vertical characteristics of reflectivity in intense convective clouds using TRMM PR data," *Environment and Natural Resources Research*, vol. 7, no. 2, p. 58, 2017.

[31] S. Kumar, "Vertical structure of precipitating shallow echoes observed from TRMM during Indian summer monsoon," *Theoretical and Applied Climatology*, vol. 133, no. 3-4, pp. 1051–1059, 2018.

[32] U. Romatschke and R. A. Houze Jr, "Extreme summer convection in South America," *Journal of Climate*, vol. 23, no. 14, pp. 3761–3791, 2010.

[33] C. Liu and E. J. Zipser, "The global distribution of largest, deepest, and most intense precipitation systems," *Geophysical Research Letters*, vol. 42, no. 9, pp. 3591–3595, 2015.

[34] M. Hirose, R. Oki, D. A. Short, and K. Nakamura, "Regional characteristics of scale-based precipitation systems from ten years of TRMM PR data," *Journal of the Meteorological Society of Japan*, vol. 87A, pp. 353–368, 2009.

[35] A. Hamada, Y. Murayama, and Y. N. Takayabu, "Regional characteristics of extreme rainfall extracted from TRMM PR measurements," *Journal of Climate*, vol. 27, no. 21, pp. 8151–8169, 2014.

[36] K. L. Rasmussen and R. A. Houze Jr, "Orogenic convection in subtropical south America as seen by the TRMM satellite," *Monthly Weather Review*, vol. 139, no. 8, pp. 2399–2420, 2011.

[37] B. Wang, Q. Ding, and J. Liu, "Concept of global monsoon," in *The Global Monsoon 650 System: Research and Forecast 3–14*, C.-P. Chang, Ed., World Scientific Publishing, Singapore, 2011.

[38] P. J. Webster, V. O. Magaña, T. N. Palmer et al., "Monsoons: processes, predictability, and the prospects for prediction," *Journal of Geophysical Research: Oceans*, vol. 103, no. C7, pp. 14451–14510, 1998.

[39] D. I. Lee, S. M. Jang, C. H You et al., "The characteristics of summer monsoon rainfall at the southwestern ocean area of Korea: a study of the 2007 season," in *The Global Monsoon System: Research and Forecast 319–338*, C.-P. Chang, Ed., World Scientific Publishing, Singapore, 2011.

[40] B. N. Goswami, M. C. Wheeler, J. C. Gottschalck, and D. E. Waliser, "Intraseasonal variability and forecasting: a review of recent research," in *The Global Monsoon System: Research and Forecast*, C.-P. Chang, Ed., pp. 389–407, World Scientific Publishing Co. Pte. Ltd, Singapore, 2nd edition, 2011.

[41] D. R. Sikka, "Synoptic and meso-scale weather disturbances over South Asia during the Southwest Summer monsoon season," in *The Global Monsoon System: Research and Forecast*, C.-P. Chang, Ed., pp. 183–204, World Scientific Publishing, Singapore, 2011.

[42] C. Kidd, "Satellite rainfall climatology: a review," *International Journal of Climatology*, vol. 21, no. 9, pp. 1041–1066, 2001.

[43] P. Xie, J. E. Janowiak, P. A. Arkin et al., "GPCP Pentad precipitation analyses: an experimental dataset based on gauge observations and satellite estimates," *Journal of Climate*, vol. 16, no. 13, pp. 2197–2214, 2003.

[44] A. Y. Hou, R. K. Kakar, S. Neeck et al., "The global precipitation measurement mission," *Bulletin of the American Meteorological Society*, vol. 95, no. 5, pp. 701–722, 2014.

[45] S. Liu, X. Mo, H. Li, G. Peng, and A. Robock, "Spatial variation of soil moisture in China: geostatistical characterization," *Journal of the Meteorological Society of Japan*, vol. 79, no. 1B, pp. 555–574, 2001.

[46] A. K. Varma and G. Liu, "Small-scale horizontal rain-rate variability observed by satellite," *Monthly Weather Review*, vol. 134, no. 10, pp. 2722–2733, 2006.

[47] A. K. Varma and G. Liu, "On classifying rain types using satellite microwave observations," *Journal of Geophysical Research: Atmospheres*, vol. 16, no. D7, p. 115, 2010.

[48] C. Liu, "Rainfall contributions from precipitation systems with different sizes, convective intensities, and durations over the tropics and subtropics," *Journal of Hydrometeorology*, vol. 12, no. 3, pp. 394–412, 2011.

[49] T. M. Rickenbach and S. A. Rutledge, "Convection in TOGA COARE: horizontal scale, morphology, and rainfall production," *Journal of the Atmospheric Sciences*, vol. 55, no. 17, pp. 2715–2729, 1998.

[50] S. P. Chavez and K. Takahashi, "Orographic rainfall hot spots in the Andes-Amazon transition according to the TRMM precipitation radar and in situ data," *Journal of Geophysical Research: Atmospheres*, vol. 122, no. 11, pp. 5870–5882, 2017.

[51] R. A. Houze, "Orographic effects on precipitating clouds," *Reviews of Geophysics*, vol. 50, no. 1, 2012.

[52] J. Houston and A. J. Hartley, "The central Andean west-slope rainshadow and its potential contribution to the origin of hyper-aridity in the Atacama Desert," *International Journal of Climatology*, vol. 23, no. 12, pp. 1453–1464, 2003.

[53] S. Medina, R. A. Houze Jr, A. Kumar, and D. Niyogi, "Summer monsoon convection in the Himalayan region: terrain and land cover effects," *Quarterly Journal of the Royal Meteorological Society: A Journal of the Atmospheric Sciences, Applied Meteorology and Physical Oceanography*, vol. 136, no. 648, pp. 593–616, 2010.

[54] H. R. Pruppacher and J. D. Klett, *Microphysics of Clouds and Precipitation*, p. 961, Kluwer Academic, Dordrecht, Netherlands, 1997.

[55] M. Konwar, R. S. Maheskumar, J. R. Kulkarni, E. Freud, B. N. Goswami, and D. Rosenfeld, "Aerosol control on depth of warm rain in convective clouds," *Journal of Geophysical Research: Atmospheres*, vol. 117, no. D13, 2012.

[56] C. Lucas, E. J. Zipser, and M. A. LeMone, "Vertical velocity in oceanic convection off tropical Australia," *Journal of the Atmospheric Sciences*, vol. 51, no. 21, pp. 3183–3193, 1994.

[57] R. Fu, B. Zhu, and R. E. Dickinson, "How do atmosphere and land surface influence seasonal changes of convection in the tropical Amazon?," *Journal of Climate*, vol. 12, no. 5, pp. 1306–1321, 1999.

[58] G. M. Heymsfield, L. Tian, A. J. Heymsfield, L. Li, and S. Guimond, "Characteristics of deep tropical and subtropical convection from nadir-viewing high-altitude airborne doppler radar," *Journal of the Atmospheric Sciences*, vol. 67, no. 2, pp. 285–308, 2010.

[59] S. Kumar, Y.-S. Vidal, A. S. Moya-Álvarez, and D. Martínez-Castro, "Effect of the surface wind flow and topography on precipitating cloud systems over the Andes and associated Amazon basin: GPM observations," *Atmospheric Research*, vol. 225, pp. 193–208, 2019.

[60] E. E. Villalobos, D. Martinez-Castro, S. Kumar, Y. Silva, and O. Fashe, "Estudio de tormentas convectivas sobre los Andes Centrales del Perú usando los radares PR-TRMM y KuPR-GPM," *Revista Cubana de Meteorología*, vol. 25, no. 1, pp. 59–75, 2019.

[61] A. S. Moya-Álvarez, D. Martínez-Castro, S. Kumar, R. Estevan, and Y. Silva, "Response of the WRF model to different resolutions in the rainfall forecast over the complex Peruvian orography," *Theoretical and Applied Climatology*, pp. 1–15, 2019.

[62] A. Moya-Álvarez, J. Gálvez, A. Holguín et al., "Extreme rainfall forecast with the WRF-ARW model in the Central Andes of Peru," *Atmosphere*, vol. 9, no. 9, p. 362, 2018.

[63] S. Lasher-Trapp, S. Kumar, D. H. Moser et al., "On different microphysical pathways to convective rainfall," *Journal of Applied Meteorology and Climatology*, vol. 57, no. 10, pp. 2399–2417, 2018.